Initial Experiences Using Deep Resolve Boost to Accelerate Whole-Body Diffusion MRI

Andrea Ponsiglione[1,2]; Will McGuire[2]; Marie Fennessy[2]; Anwar R. Padhani[2]

[1]Department of Advanced Biomedical Sciences, University of Naples Federico II, Naples, Italy
[2]Paul Strickland Scanner Centre, Mount Vernon Cancer Centre, Northwood, Middlesex, United Kingdom

Introduction

In the last decade, whole-body MRI (WB-MRI) has become established as a non-invasive imaging technique for staging and response assessment of cancers with a predilection to spread to the bone [1–3], with emerging indications for screening and inflammatory conditions [4, 5].

Diffusion-weighted imaging (DWI) represents a core sequence [1, 4, 6] achieving on modern MRI scanners spatial resolutions able to detect small lesions up to 5 mm in size with good image quality. The sequence is sensitive to tissue cellularity and water diffusivity while enabling quantification of the apparent diffusion coefficient (ADC; unit: $\mu m^2/s$), which aids in lesion characterization and treatment response evaluations [7].

WB-DWI is performed through a series of sequential imaging stations, usually from the head to the mid-thighs, with each station consisting of 30–50, 5-mm thick axial sections and images generally acquired by using two diffusion weightings (50–800/1000 s/mm^2) [8]. Because scanning each station takes approximately 3 minutes, WB-DWI accounts for approximately half of the total acquisition time of a WB-MRI study.

Due to the increasing demand for WB-MRI exams, reducing acquisition times while maintaining image quality would enable greater adoption in clinical routine and improve patient experience [9].

Deep Resolve Boost (DRB) is a raw data-to-image deep-learning reconstruction technology by Siemens Healthineers that enables accelerated image acquisition with high signal-to-noise (SNR) images by increasing parallel imaging acceleration (PAT) factors and/or reducing the number of acquired averages [10].

In this case-based review, we share our initial experience with the DRB WB-DWI sequence in comparison with the sequence that we use routinely, focusing on quantitative and qualitative findings assessed on axial b900 and the corresponding MIP images. The conventional and DRB WB-DWI acquisition protocols for our 1.5T MAGNETOM Sola machine are listed in Table 1.

	Conventional whole-body DWI	DRB whole-body DWI
Scan plane	Axial	Axial
Diffusion mode	3-scan trace	3D diagonal
Diffusion scheme	Bipolar	Monopolar
TR (ms)	6170	5370
TE (ms)	74	63
FOV (mm)	430	430
Phase FOV (% of FOV)	87.5	90.6
Slices	40	40
Slice thickness (mm)*	5	5
Matrix (interpolated matrix)	128 × 128 (256 × 256)	128 × 128 (256 × 256)
Fat suppression method (inversion time, ms)	Inversion recovery (180)	Inversion recovery (180)
Phase encoding direction	A > P	A > P
iPAT	2	3
b-values (s/mm^2)	50–900	50–900
Averages (3D diagonal equivalence)	2, 6 (6, 18)	3, 8 (3, 8)
Bandwidth (Hz/pixel)	2298	1954
Adjustment strategy	SliceAdjust	SliceAdjust
DL reconstruction	N/A	DRB
Denoising strength	N/A	Normal
Acquisition time (min:s)	2:48 (× 5 stations)	1:17 (× 5 stations)

Table 1: Technical parameters of the whole-body DWI acquisition protocols.
*without spacing; DRB: Deep Resolve Boost, TR: repetition time, TE: echo time, FOV: field of view, iPAT: integrated parallel acquisition technique, DL: deep learning

Case 1

A 66-year-old postmenopausal woman presented with bone and lung metastases from breast carcinoma (HER2-positive) on Trastuzumab emtansine therapy. She was referred for WB-MRI to assess her disease status (Figures 1 and 2).

Quantitative assessment
Axial b900 DRB-DWI shows a higher SNR (calculated as signal intensity divided by standard deviation of background air noise adjacent to the lateral chest wall) than the conventional sequence at different anatomical sites, including the parietal cerebral white matter (251 vs. 189 AU), third lumbar vertebral body (91 vs. 33 AU), and spleen (171 vs. 51 AU).

Two different metastatic lesions are chosen for further assessment: within the left lung and at the level of the second lumbar vertebra. The SNR results are higher for DRB-DWI (151 and 178 vs. 48 and 111 AU, respectively), whereas the mean ADC values ($\mu m^2/s$) are similar (1457 and 1194 vs. 1463 and 1221 $\mu m^2/s$).

Qualitative assessment
Axial b900 DRB-DWI shows better white/gray matter zone differentiation, with an overall greater signal intensity for visceral organs and bones. When assessing the metastatic lesions, both are visualized with higher conspicuity in the axial DRB sequence. When evaluating the presence of artifacts, axial b900 DRB-DWI shows fewer near-field artifacts.

As for MIP images (Fig. 2), the DRB exhibits a more homogenous background fat suppression in both the frontal and lateral views, with fewer artifacts from the edematous right breast, which compromises the visibility of the chest lesions on the projections for the conventional images. The transitions between different stations are also less evident in the DRB MIP images, whereas striping artifacts are equally visible in both protocols (upper spleen on the conventional images and lower spleen on the DRB images). Both the lung and spine deposits are better depicted on DRB MIP images.

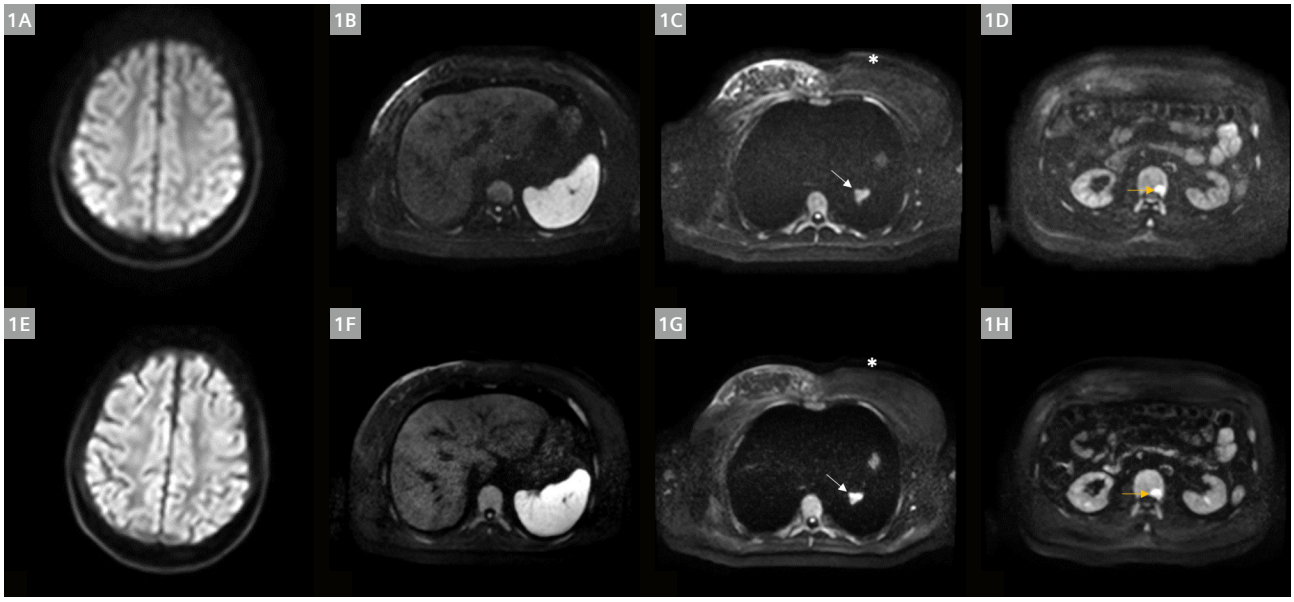

1 Axial b900 DW images in conventional **(1A–D)** and DRB protocols **(1E–H)** from a 66-year-old postmenopausal woman presenting with bone and lung metastatic breast carcinoma (HER2-positive) and increased bilirubin, on trastuzumab emtansine. The DRB images show better white/grey matter zone differentiation, with higher signal intensity for the liver, spleen, and lumbar spine compared to the conventional ones. Greater near-field artifacts (*) are present in the conventional images, whereas lung and lumbar spine metastatic lesions (arrows) are visualized with higher conspicuity in the axial DRB sequence.

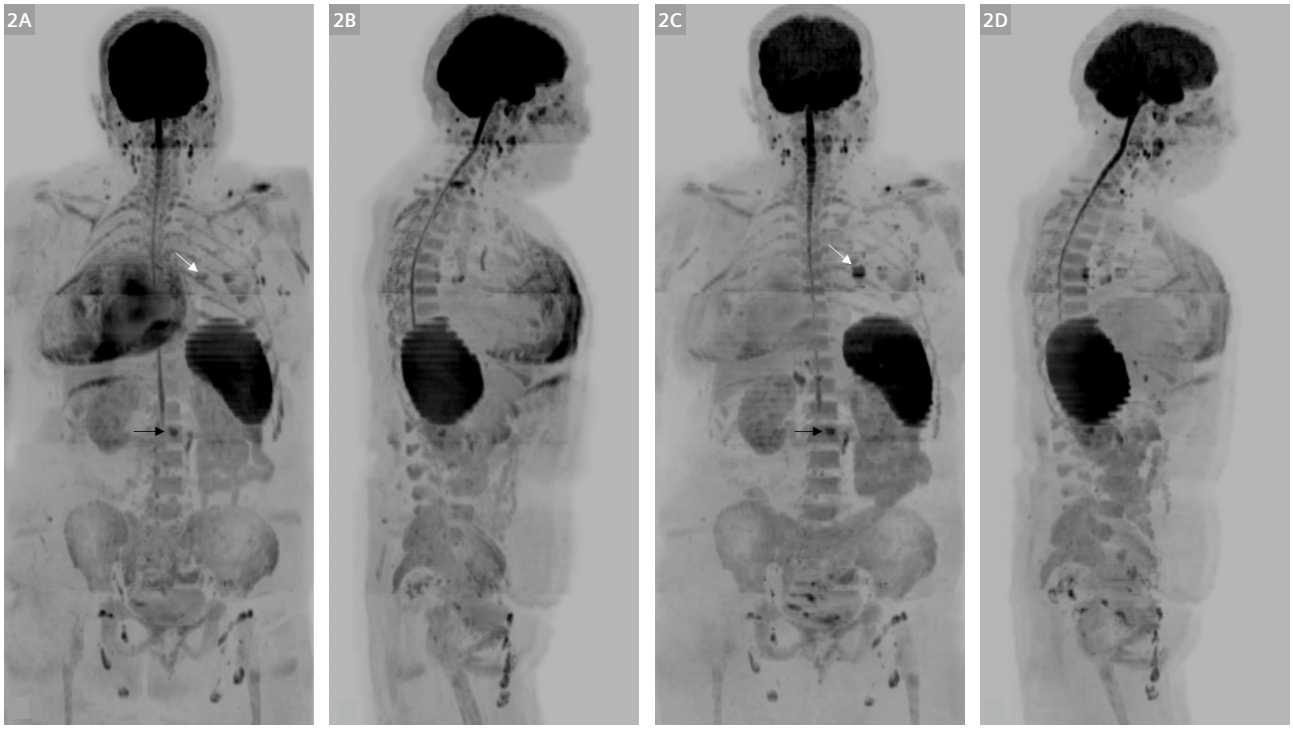

2 Frontal and lateral views of whole-body b900 3D MIP (inverted greyscale) of conventional **(2A, B)** and DRB protocols **(2C, D)**. The DRB MIP shows a more homogenous background fat suppression on both projections, with fewer artifacts from the right breast area. The transition between different stations is less evident on the DRB MIPs while striping artefacts are equally visible in both protocols (upper spleen on the conventional images and lower spleen on the DRB images). Lung and lumbar spine metastatic lesions (arrows) are better depicted on the DRB MIP.

Case 2

A 67-year-old man presented with diffuse bone metastatic prostate cancer and increased serum prostate-specific antigen (PSA) levels on anti-androgen therapy. He was referred for WB-MRI to assess his disease status (Figures 3 and 4).

Quantitative assessment

Both axial b900 DWI sequences show similar SNR at the level of parietal brain white matter (104 vs. 101 AU), while DRB exhibits a higher SNR than the conventional sequence when assessing the spleen (166 vs. 99 AU).

Regarding the two metastatic lesions chosen as targets in the 9th thoracic vertebra and the left posterior acetabulum, the SNR results are higher for DRB-DWI (201 and 239 vs. 151 and 143 AU, respectively), whereas the mean ADC values are similar (765 and 780 vs. 750 and 734 $\mu m^2/s$, respectively).

Qualitative assessment

Axial b900 DRB-DWI exhibits improved white/gray matter zone differentiation, with an overall higher image contrast for visceral organs and bone. Notably, both liver lobes and the pancreas show greater signal intensity compared to conventional acquisition. The conspicuity of metastatic lesions is equivalent. As for the presence of artifacts, axial b900 DRB-DWI shows fewer near-field artifacts than the conventional sequence.

Regarding MIP images, DRB shows more uniform background fat suppression on both frontal and lateral projections. Transitions between the image block stations are slightly more evident in conventional DWI, whereas striping artifacts in the abdominal stations are more evident in the DRB images. The conspicuity of target metastatic lesions is equivalent.

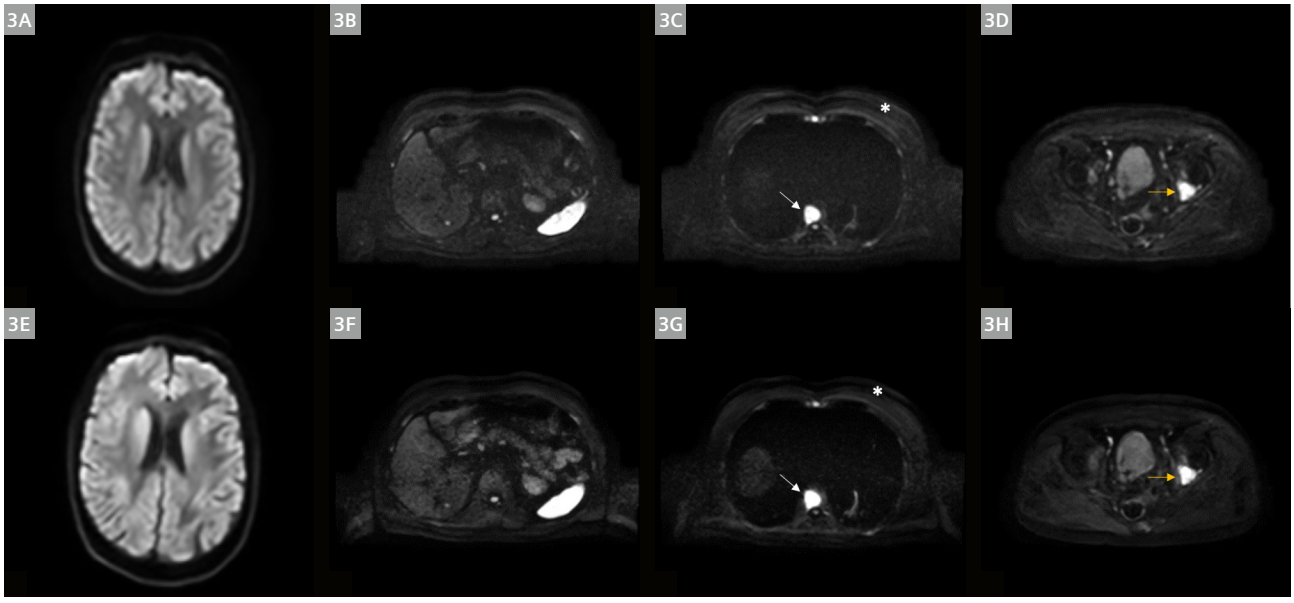

3 Axial b900 DW images in conventional **(3A–D)** and DRB protocols **(3E–H)**, from a 67-year-old man presenting with diffuse bone metastatic prostate cancer, with rising PSA values on androgen deprivation therapy. The DRB images exhibit a greater white/grey matter zone differentiation, with improved sharpness for the liver, pancreas as well as lumbar spine compared to the conventional ones. Near-field artefacts (*) are less evident in the DRB image, while the conspicuity for both the 9th thoracic vertebra and left posterior acetabulum metastatic lesions (arrows) is the same across different protocols.

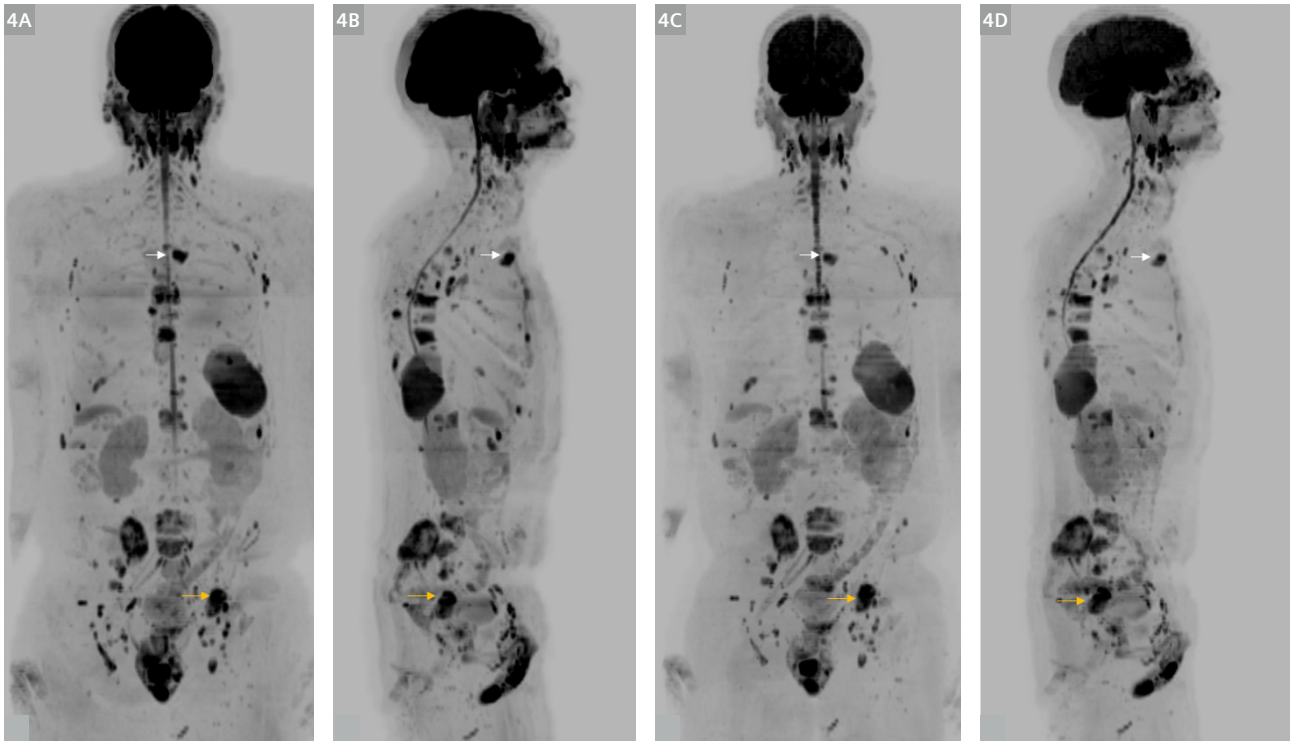

4 Frontal and lateral view of whole-body b900 3D MIP (inverted scale) in conventional **(4A, B)** and DRB protocols **(4C, D)**. The DRB MIP shows better background fat suppression either on frontal or lateral views, with the transition between different stations being slightly less evident. Striping artefacts within abdomen stations are more evident in the DRB sequence. Multiple bone metastases can be appreciated, in particular, both the 9th thoracic vertebra and left posterior acetabulum deposits chosen as targets show similar conspicuity across protocols (arrows).

Case 3

An 84-year-old woman presented with lung, bone, and liver metastatic breast carcinoma (ER-positive and HER2-negative) after receiving palbociclib and hormonal therapy. She was referred for worsening overall performance status accompanied by breathlessness, and for a WB-MRI scan to assess the extent of her disease (Figures 5 and 6).

Quantitative assessment

Axial b900 DRB-DWI shows a higher SNR than the conventional sequence at different anatomical sites, including the brain white matter (235 vs. 188 AU), third lumbar vertebra (38 vs. 22 AU), and spleen (129 vs. 44 AU).

Two metastatic lesions are chosen as targets: one in the right subpleural lung base and one in the left sacrum. In the axial DRB-DWI, they show higher SNR (152 and 201 vs. 54 and 137 AU, respectively), with minimally lower mean ADC values (915 and 977 vs. 1130 and 1091 $\mu m^2/s$) compared to the conventional sequence. The difference in the ADC values is within the repeatability coefficient limits for ADC values [11].

Qualitative assessment

Axial b900 DRB-DWI shows better white/gray matter zone differentiation, with overall similar visualization quality for visceral organs, and slightly better sharpness for the spine.

The conspicuity of the right subpleural lesion is higher for the DRB sequence, whereas that of the left sacrum is equivalent. When evaluating the presence of artifacts, axial b900 DRB-DWI shows larger artifacts through the thorax related to breast implants. However, in this case, where deposits are widespread in both lungs, artifacts do not compromise the overall diagnostic assessment. Furthermore, the patient underwent a left hip replacement, and the related artifacts are equivalent in both sequences.

Regarding the MIP images, DRB shows similar background fat suppression in frontal and lateral views. Similarly, the transition between different stations is also equivalent, whereas striping artifacts are slightly more evident in the DRB sequence. Bilateral breast implants cause larger artifacts in the lateral MIP for the DRB sequence; however, artifacts related to the metallic left hip prosthesis are the same. Finally, the conspicuity of the right lung lesion is slightly higher for the DRB sequence, whereas that of the left sacrum deposit is equivalent across the protocols.

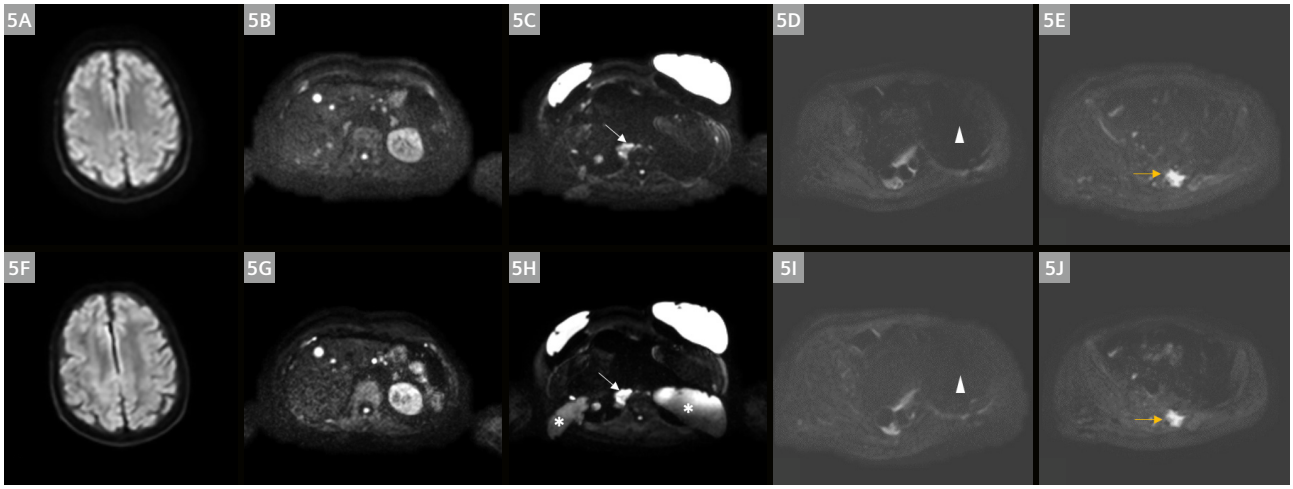

5 Axial b900 DW images in conventional **(5A–E)** and DRB protocols **(5F–J)**, from an 84-year-old woman presenting with extensive lung, bone, and liver metastatic breast carcinoma (HR-positive and HER2-negative) on Palbociclib. The DRB images exhibit greater white/grey matter zone differentiation, with similar sharpness for visceral organs and the lumbar spine. Axial b900 DRB-DWI shows greater artefacts through the thorax station related to bilateral breast implants (asterisks) compared to the conventional sequence, although the diagnostic assessment of the widespread lung deposits is maintained. Artifacts from left hip replacement (arrowheads) are equivalent across protocols. The conspicuity of the right lung subpleural lesion is higher for the DRB sequence (white arrows) compared to the conventional one, while that of the left sacrum is equivalent (orange arrows).

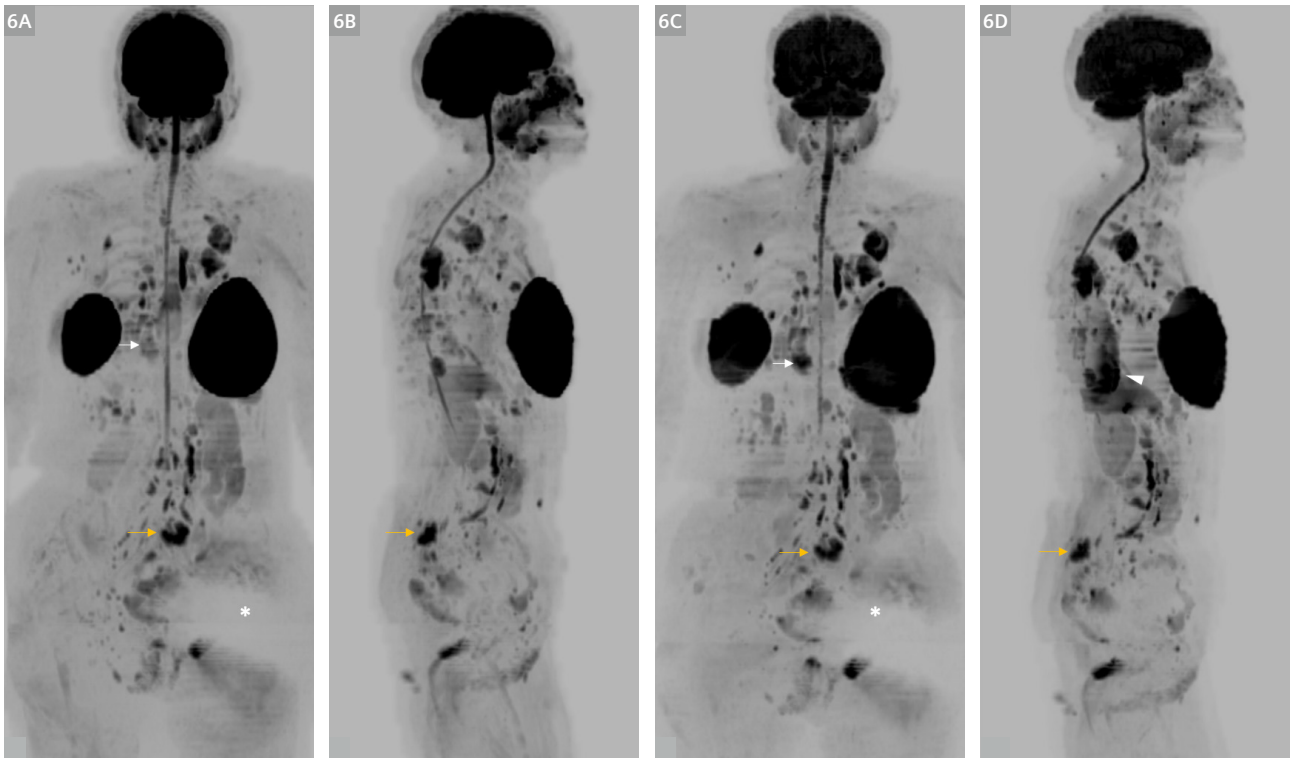

6 Frontal and lateral projections of whole-body b900 3D MIP (inverted scale) in the conventional **(6A, B)** and DRB protocols **(6C, D)**. The DRB MIP showed similar fat background suppression on both the frontal and lateral views compared to the conventional MIP. The transition between different stations is equivalent while stripping artifacts within abdominal stations are slightly more evident in the DRB sequence. Artifacts from the bilateral breast implants are greater in the lateral AI MIP (arrowhead), while those related to the left hip prosthesis are the same (asterisks in frontal projections). The conspicuity of the right subpleural lesion is higher for the DRB sequence (white arrows in the frontal projections) than for the conventional sequence, while that of the left sacrum deposit is equivalent (orange arrows).

Conclusion

Our experience with 50 head-to-head comparisons of DRB-DWI with a conventional sequence in the context of WB imaging shows that the optimized DRB sequence from Siemens Healthineers produces high-quality axial images resulting in improved MIP projections, while at the same time reducing the acquisition time by more than half. DRB-DWI is superior or equivalent to the conventional sequence in terms of overall SNR and lesion conspicuity on axial images, with more uniform background fat suppression on MIP projections. However, increased striping artifacts in the abdomen, and artifacts related to silicone breast implants should be further investigated for their clinical impact. The time-saving with preserved image quality allowed us to incorporate a modified DRB-DWI sequence into our clinical routine to increase patient throughput.

References

1 Messiou C, Hillengass J, Delorme S, Lecouvet FE, Moulopoulos LA, Collins DJ, et al. Guidelines for Acquisition, Interpretation, and Reporting of Whole-Body MRI in Myeloma: Myeloma Response Assessment and Diagnosis System (MY-RADS). Radiology. 2019;291(1):5-13.
2 Ahlawat S, Debs P, Amini B, Lecouvet FE, Omoumi P, Wessell DE. Clinical Applications and Controversies of Whole-Body MRI: AJR Expert Panel Narrative Review. AJR Am J Roentgenol. 2023;220(4):463-475.
3 Cruz IAN, Fayad LM, Ahlawat S, Lederman HM, Nico MAC, Ormond Filho AG, et al. Whole-Body MRI in Musculoskeletal Oncology: A Comprehensive Review with Recommendations. Radiol Imaging Cancer. 2023;5(3):e220107.
4 Petralia G, Koh DM, Attariwala R, Busch JJ, Eeles R, Karow D, et al. Oncologically Relevant Findings Reporting and Data System (ONCO-RADS): Guidelines for the Acquisition, Interpretation, and Reporting of Whole-Body MRI for Cancer Screening. Radiology. 2021;299(3):494-507.
5 Kraus MS, Yousef AA, Cote SL, Greer MC. Improving protocols for whole-body magnetic resonance imaging: oncological and inflammatory applications. Pediatr Radiol. 2023;53(7):1420-1442. Epub 2022 Aug 19.

6 Padhani AR, Lecouvet FE, Tunariu N, Koh DM, De Keyzer F, Collins DJ, et al. METastasis Reporting and Data System for Prostate Cancer: Practical Guidelines for Acquisition, Interpretation, and Reporting of Whole-body Magnetic Resonance Imaging-based Evaluations of Multiorgan Involvement in Advanced Prostate Cancer. Eur Urol. 2017;71(1):81-92.
7 Tunariu N, Blackledge M, Messiou C, Petralia G, Padhani A, Curcean S, et al. What's New for Clinical Whole-body MRI (WB-MRI) in the 21st Century. Br J Radiol. 2020;93(1115):20200562.
8 Petralia G, Padhani AR. Whole-Body Magnetic Resonance Imaging in Oncology: Uses and Indications. Magn Reson Imaging Clin N Am. 2018;26(4):495-507.
9 Evans RE, Taylor SA, Beare S, Halligan S, Morton A, Oliver A, et al. Perceived patient burden and acceptability of whole-body MRI for staging lung and colorectal cancer; comparison with standard staging investigations. Br J Radiol. 2018;91(1086):20170731.
10 Siemens Healthineers. Deep Resolve Boost [Internet]. Erlangen, Germany: Siemens Healthcare GmbH [Accessed on June 7, 2023]. Available from: https://www.siemens-healthineers.com/magnetic-resonance-imaging/options-and-upgrades/clinical-applications/deep-resolve-boost
11 ElGendy K, Barwick TD, Auner HW, Chaidos A, Wallitt K, Sergot A, et al. Repeatability and test-retest reproducibility of mean apparent diffusion coefficient measurements of focal and diffuse disease in relapsed multiple myeloma at 3T whole body diffusion-weighted MRI (WB-DW-MRI). Br J Radiol. 2022;95(1138):20220418.

Contact

Dr. Andrea Ponsiglione, Ph.D.
Post-doctoral Research Fellow
Department of Advanced Biomedical Sciences
University of Naples Federico II
Via Pansini 5
Napoli, 80131
Italy
Tel.: +39 (0)817 464 857
a.ponsiglionemd@gmail.com

Will McGuire
Deputy Superintendent Radiographer
Paul Strickland Scanner Centre
Rickmansworth Road
Northwood, Middlesex HA6 2RN
United Kingdom
Tel.: +44 (0)1923 886 310
will.mcguire@stricklandscanner.org.uk

Prof. Anwar R. Padhani,
MB, BS, FRCP, FRCR
Consultant Radiologist and
Professor of Cancer Imaging
Paul Strickland Scanner Centre
Mount Vernon Cancer Centre
Rickmansworth Road
Northwood, Middlesex HA6 2RN
United Kingdom
Tel. (PA): +44 (0)1923 844 751
anwar.padhani@stricklandscanner.org

Marie Fennessy
MRI Superintendent Radiographer
Paul Strickland Scanner Centre
Rickmansworth Road
Northwood, Middlesex HA6 2RN
United Kingdom
Tel.: +44 (0)1923 886 310
marie.fennessy@stricklandscanner.org.uk